PHYSICAL REVIEW A **104**, 043510 (2021)

Topological and hyperbolic dielectric materials from chirality-induced charge-parity symmetry

Junpeng Hou,[1] Zhitong Li,[2] Qing Gu,[2] and Chuanwei Zhang[1,*]
[1]*Department of Physics, University of Texas at Dallas, Richardson, Texas 75080-3021, USA*
[2]*Department of Electrical and Computer Engineering, University of Texas at Dallas, Richardson, Texas 75080-3021, USA*

(Received 12 April 2021; revised 17 September 2021; accepted 21 September 2021; published 12 October 2021)

Parity-time ($\mathcal{PT}$) symmetry, originally conceived for non-Hermitian open quantum systems, has opened an exciting avenue towards coherent control of light for significant applications. Here we propose a paradigm towards non-Hermitian photonics based on the charge-parity ($\mathcal{CP}$) symmetry, in which the charge conjugation and parity symmetries are broken individually but preserved jointly. Such a symmetry-breaking scheme induces a transition from dielectric to hyperbolic dispersions in chiral dielectrics, leading to lossless all-dielectric hyperbolic metamaterials. More interestingly, the $\mathcal{CP}$-symmetry transition represents a non-Hermitian topological phase transition that occurs at infinite energy and requires no explicit band gap closing. We further showcase broad applications of $\mathcal{CP}$-symmetric photonics such as an all-angle polarization-dependent beam splitter and enhanced spontaneous emission. The $\mathcal{CP}$ symmetry opens an unexplored pathway for non-Hermitian topological photonics by bringing new physics into strong chiral metamaterials, therefore providing a powerful tool for engineering many promising applications in photonics and other related fields.

DOI: 10.1103/PhysRevA.104.043510

I. INTRODUCTION

Originally conceived for open quantum systems [1], $\mathcal{PT}$ symmetry was later introduced to photonics through the analogy between the Schrödinger equation and Maxwell equations under paraxial approximation [2,3]. $\mathcal{PT}$ symmetry allows a real eigenspectrum for a class of non-Hermitian Hamiltonians [3,4], which support two distinct phases: $\mathcal{PT}$ symmetric (real eigenfrequencies) and $\mathcal{PT}$ broken (both real and complex eigenfrequencies), as illustrated in Fig. 1(a). The phase transition between them is characterized by the exceptional point [5]. In photonics, a non-Hermitian Hamiltonian with $\mathcal{PT}$ symmetry can be engineered through tuning optical gain and loss of materials, which provides a powerful tool for shaping the flow of light and yields novel applications in nonlinear optics [6], lasing [7,8], unidirectional propagation [9], precise sensing [10], topological photonics [11,12], etc.

The significance of $\mathcal{PT}$-symmetric photonics naturally raises the question of whether there is non-Hermitian photonics protected by other types of symmetries. The $\mathcal{PT}$ symmetry for photonics is generally based on the paraxial approximation of Maxwell equations, which describe the multiple-component electromagnetic field and could be non-Hermitian even without optical gain or loss. This can be seen from the fact that the Maxwell equation may exhibit a complex spectrum in common media with only real permittivity or permeability vectors. For example, the complex spectra in metals are closely related to interesting phenomena like surface plasmon polaritons and skin effects [13,14]. However, the complex spectra in metals are not protected by any symmetry and can be connected to real spectra in dielectrics through a zero-index point, at which the refractive index becomes zero [15–18].

In this article, we propose a class of non-Hermitian photonics based on the $\mathcal{CP}$ symmetry of Maxwell equations, where $\mathcal{C}$ represents charge conjugation. There are two distinct phases: $\mathcal{CP}$ symmetric with real eigenfrequencies and $\mathcal{CP}$ broken with complex eigenfrequencies. Such $\mathcal{CP}$-symmetric non-Hermitian photonics can exist, for instance, in a continuous dielectric medium with proper chiral effects. An example is provided in Fig. 1(b), where the spectra are twofold degenerate. The transition between $\mathcal{CP}$-symmetric and -broken phases can occur at points, lines, or surfaces in either parameter or momentum space. The transition points are analogous to the exceptional points in $\mathcal{PT}$ symmetry in the sense of defective Hamiltonians; therefore, we still name them exceptional points. However, at the exceptional points, the eigenfrequencies (both real and imaginary parts) diverge [Fig. 1(b)] for the $\mathcal{CP}$ symmetry, in contrast to the degeneracy at finite values for the $\mathcal{PT}$ symmetry [see Fig. 1(a) and Appendix A].

The transition between $\mathcal{CP}$-symmetric and -broken phases is accompanied by a dramatic change in the photonic band topology. In the $\mathcal{CP}$-symmetric phase, the band is still dielectric, with elliptical equal-frequency surfaces (EFSs), while in the $\mathcal{CP}$-broken phase, the band dispersion becomes hyperbolic, with indefinite bands. The hyperbolic band dispersion is considered to be a unique feature of hyperbolic metamaterials (HMMs) [19,20], which are usually implemented by creating a metal-dielectric composite to achieve metal and dielectric properties in orthogonal directions. HMMs have found great applications in versatile fields like negative refraction [21,22], enhanced spontaneous emission [23–27], superresolution imaging [28,29], biosensing [30], control of critical coupling [31], and topological photonics [32–34]. However, a fundamental challenge that hinders the applications of

---

[*] chuanwei.zhang@utdallas.edu

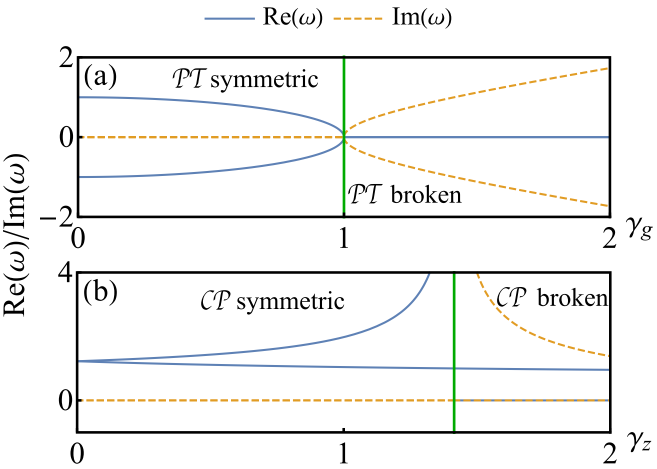

FIG. 1. Eigenfrequency spectra for non-Hermitian photonics with (a) $\mathcal{PT}$ and (b) $\mathcal{CP}$ symmetries. Solid blue and dashed orange curves represent the real and imaginary parts of the eigenfrequencies. For the $\mathcal{CP}$ case, each curve is twofold degenerate with different eigenstates. The green vertical lines indicate the exceptional points, at which the Hamiltonian is defective. The driving terms for the symmetry breaking are on-site gain and loss γ_g and the chiral effect along the z direction γ_z. At the exceptional point, a pair of eigenmodes becomes degenerate at $\omega = 0$ for $\mathcal{PT}$ symmetry breaking (see also Appendix A) but diverges for $\mathcal{CP}$ symmetry breaking. The spectrum for the latter case is computed in a chiral dielectric $\epsilon = 2$ and $\mu = 1$.

HMMs is their large rates of dissipation originating from the metal constitutions. In previous works, active composites were added [35,36] in order to compensate the loss.

In this article, we illustrate the $\mathcal{CP}$-symmetry-based non-Hermitian photonics and the associated change in photonic band topology using dielectrics with strong anisotropic chirality. Such a chirality-driven transition from $\mathcal{CP}$-symmetric to $\mathcal{CP}$-broken phases provides a route to realize hyperbolic materials in all-dielectric media, leading to lossless *all-dielectric hyperbolic materials*. More interestingly, the $\mathcal{CP}$-breaking transition is a topological one that occurs at infinite energy and requires no band gap closing and reopening; therefore, it represents a class of non-Hermitian continuous topological materials with rich physics. The $\mathcal{CP}$-symmetric non-Hermitian physics enables broad and promising technological applications due to the unique combination of non-Hermitian topological phases and lossless hyperbolic bands. In this work, we showcase two relevant device applications: all-angle polarization-dependent negative refraction for optical control and enhanced spontaneous emission for lasing.

II. NON-HERMITIAN PHOTONICS BASED ON $\mathcal{CP}$ SYMMETRY

A. Symmetries of Maxwell's equations

We consider a continuous photonic medium that can be described by Maxwell's equations in the extended eigenvalue-problem form $H_P\psi = \omega H_M\psi$, with

$$H_P = i\begin{pmatrix} 0 & \nabla\times \\ -\nabla\times & 0 \end{pmatrix},\quad H_M = \begin{pmatrix} \epsilon & i\gamma \\ -i\gamma & \mu \end{pmatrix},\quad \psi = \begin{pmatrix} \boldsymbol{E} \\ \boldsymbol{H} \end{pmatrix}. \tag{1}$$

TABLE I. Symmetries of Maxwell equations. Some important symmetries, together with their actions on eigenmodes and breaking methods, are listed for $H(\boldsymbol{k})$. Besides $\mathcal{CPT}$, two symmetries, $H(\boldsymbol{k}) = -H(\boldsymbol{k})$ and $\mathcal{P}\Gamma$, are always preserved.

Symmetry	Eigenmodes	Breaking mechanism(s)
$\mathcal{T}$	$\omega_k \rightarrow \omega^*_{-k}$	Gain or loss, gyromagnetic
$\mathcal{C}$	$\omega_k \rightarrow \omega^*_k$	Gain or loss, chiral, gyromagnetic
$\mathcal{C}\Gamma$	$\omega_k \rightarrow \omega^*_k$	Gain or loss, gyromagnetic
$\mathcal{P}$	$\omega_k \rightarrow \omega_{-k}$	Chiral
$\mathcal{P}\Gamma$	$\omega_k \rightarrow \omega_{-k}$	Cannot be broken

Here the chiral term $\gamma = \mathrm{Tr}(\gamma)I_3/3 + N$ [37] couples $\boldsymbol{E}$ ($\boldsymbol{D}$) and $\boldsymbol{B}$ ($\boldsymbol{H}$), I_3 is the 3×3 identity matrix, and N is a symmetric traceless matrix. For a homogeneous medium, $H(-\boldsymbol{k}) = -H(\boldsymbol{k})$, with $H(\boldsymbol{k}) = H_M^{-1}H_P(\boldsymbol{k})$ [34], dictating that eigenmodes $\omega_{\boldsymbol{k}}$ and $-\omega_{-\boldsymbol{k}}$ represent the same physical state.

The time-reversal symmetry operator is defined as $\mathcal{T} = \sigma_z \otimes I_3K$, where the Pauli matrix σ_i is defined on the $(\boldsymbol{E}, \boldsymbol{H})$ basis [38]. Such a definition transforms all the physical quantities correctly when the chiral effect is absent [39] and $\mathcal{T}^2 = 1$ as photons obey Bose-Einstein statistics. Note that time-reversal symmetry breaking is not equivalent to nonreciprocity, although the spectrum can be complex in a time-reversal-symmetric system [39]. Preserving $\mathcal{T}$ symmetry requires $\epsilon^* = \epsilon$, $\mu^* = \mu$; therefore, the gyromagnetic effect or material gain or loss breaks time-reversal symmetry. The parity symmetry operator $\mathcal{P} = -\sigma_z \otimes I_3$ satisfies $\mathcal{P}H_P(\boldsymbol{k})\mathcal{P}^{-1} = H_P(-\boldsymbol{k})$, $\det(\mathcal{P}) = -1$, and $\mathcal{P}\binom{\boldsymbol{E}}{\boldsymbol{H}} = \binom{-\boldsymbol{E}}{\boldsymbol{H}}$, as expected. The Hamiltonian $H(\boldsymbol{k})$ has an even parity, $\mathcal{P}H(-\boldsymbol{k})\mathcal{P}^{-1} = H(\boldsymbol{k})$, when $\gamma = 0$, and the parity operator changes the sign of the chirality γ [37]. Because photons are gauge bosons without mass and charge, the charge conjugation is defined as $\mathcal{C} = -K$ such that $\mathcal{CPT} = 1$ [40].

In an ideal dielectric, HMM, or metal that has only real permittivity and permeability vectors, these three symmetries are persevered individually. While each of them can be broken explicitly, $\mathcal{CPT} = 1$ is always preserved. Note that the chiral term $\gamma = \omega g$ [41]; thus, the signs of eigenfrequency and chiral term are not independent. A chiral inversion operator $\Gamma : \gamma \rightarrow -\gamma$ can be defined, which yields an additional symmetry $(\mathcal{P}\Gamma)H(\boldsymbol{k})(\mathcal{P}\Gamma)^{-1} = -H(\boldsymbol{k})$, dictating that there are only two independent nonzero modes. Hereafter, we choose both modes with $\mathrm{Re}(\omega) > 0$ (< 0) for a given chiral term γ $(-\gamma)$ [34]. The above symmetries of Maxwell's equations and their consequences are summarized in Table I.

Interesting physics arises when a combination of two symmetries, such as $\mathcal{PT}$ or $\mathcal{CP}$, is preserved while each is individually broken. Here we consider non-Hermitian photonics based on $\mathcal{CP}$ symmetry. Consider the two eigenmodes $\psi_{j,\boldsymbol{k}}$ with eigenfrequencies $\omega_{j,\boldsymbol{k}}$, $j = 0, 1$, of Maxwell's equations. Under $\mathcal{CP}$ symmetry, $(\mathcal{CP})H(\boldsymbol{k})(\mathcal{CP})^{-1} = H(-\boldsymbol{k})$, meaning $\omega^*_{j,-\mathbf{k}}$ is also an eigenfrequency. Notice that the constantly preserved $(\mathcal{P}\Gamma)H(\boldsymbol{k})(\mathcal{P}\Gamma)^{-1} = H(-\boldsymbol{k})$ symmetry yields $\omega_{j,\boldsymbol{k}} = \omega_{j,-\boldsymbol{k}}$. Such a constraint always applies and gives rise to the twofold degeneracy in Fig. 1(b).

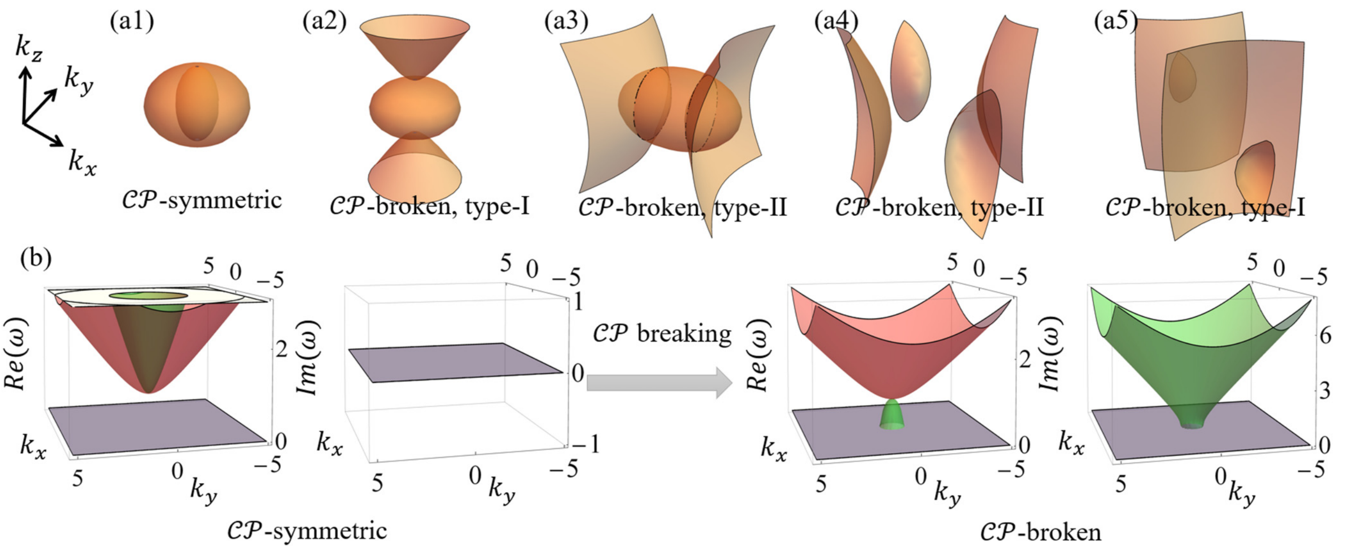

FIG. 2. $\mathcal{CP}$ breaking and hyperbolicity. (a) Some examples of EFSs at $\omega = 1$ in $\mathcal{CP}$-symmetric and -broken regions. We define the type-I and type-II HMMs according to $\det(H_M) < 0$ and $\det(H_M) > 0$, respectively. From left to right, we choose $\gamma = \mathrm{diag}(0, 0, 1)$, $\gamma = \mathrm{diag}(0, 0, 2)$, $\gamma = \mathrm{diag}(0, 2, 2)$, $(\gamma_x, \gamma_y, \gamma_{xy}, \gamma_{yx}) = (1, 1, 3, 3)$, and $(\gamma_x, \gamma_y, \gamma_z, \gamma_{xy}, \gamma_{yx}) = (1, 1, 2, 3, 3)$. (b) Dielectric real bands in (a1) change to type-I hyperbolic complex bands in (a2) across $\mathcal{CP}$ symmetry breaking in momentum space $k_z = 1$. For all panels, $\epsilon_D = 2$, and $\mu_D = 1$.

In the $\mathcal{CP}$-symmetric regime, the combination of the two conditions above gives $\omega_{j,\boldsymbol{k}} = \omega^*_{j,-\boldsymbol{k}} = \omega^*_{j,\boldsymbol{k}}$, which imposes the reality of the eigenfrequency spectrum. In this symmetric regime, the eigenstates also obey the transformation relation given by the $\mathcal{CP}$ symmetry, i.e., $(\mathcal{CP})\psi_{j,\boldsymbol{k}} = e^{i\theta_j}\psi_{j,-\boldsymbol{k}}$. $\mathcal{CP}$-broken regimes, where $\mathcal{CP}$ symmetry relates two states for a given j at the same, instead of opposite, momenta, also exist. This leads to the constraints on eigenstates $(\mathcal{CP})\psi_{j,\pm\boldsymbol{k}} = e^{i\theta_{j,\pm\boldsymbol{k}}}\psi_{j,\pm\boldsymbol{k}}$, meaning the eigenfrequencies must be purely imaginary since $\omega_{j,\pm\boldsymbol{k}} = -\omega^*_{j,\pm\boldsymbol{k}}$.

B. $\mathcal{CP}$-symmetric photonics in chiral media

The chiral term γ breaks $\mathcal{C}$ and $\mathcal{P}$ symmetries individually but preserves the combined $\mathcal{CP}$ symmetry; therefore, chiral media provide an excellent platform for exploring non-Hermitian photonics based on $\mathcal{CP}$ symmetry. Chirality is ubiquitous in many different materials, and in photonics chirality gives rise to unique wave propagations [41]. However, chiral effects are usually weak in natural materials. Recently, rapid development of chiral metamaterials [42–45] and chiral plasmonics [46] has opened the door for realizing strong chiral media in a wide range of frequencies, including microwave, terahertz [47], infrared, and visible frequencies. Besides enhanced circular dichroism and optical activity [42–44,46], strong chiral media also exhibit negative refraction for certain incident angles [48–52].

For better illustration of $\mathcal{CP}$-symmetry effects, we consider an isotropic dielectric $\epsilon = \epsilon_D I_3, \epsilon_D \geqslant 0$, $\mu = \mu_D I_3, \mu_D > 0$ with only a real diagonal chiral term $\gamma = \mathrm{diag}(\gamma_x, \gamma_y, \gamma_z)$. Such a chiral term breaks $\mathcal{C}$ and $\mathcal{P}$ but preserves their combination $\mathcal{CP}$ (see Table I). A simple, but instructive, case is $\gamma = \mathrm{diag}(0, 0, \gamma_z > 0)$. The EFS can be determined by

$$\epsilon_D\mu_D\left(k_t^2 + k_z^2 - \epsilon_D\mu_D\omega^2\right)^2 = \gamma_z^2\left(k_z^2 - \epsilon_D\mu_D\omega^2\right)^2, \qquad (2)$$

which has four solutions in general,

$$k_z = \pm\sqrt{f_\pm(\gamma_z)k_t^2 + \omega^2\epsilon_D\mu_D}, \qquad (3)$$

where $f_\pm(\gamma_z) = \frac{\sqrt{\epsilon_D\mu_D}}{\pm\gamma_z - \sqrt{\epsilon_D\mu_D}}$ and $k_t^2 = k_x^2 + k_y^2$.

For a small $\gamma_z < \sqrt{\epsilon_D\mu_D}$, $f_\pm(\gamma_z)$ are both negative; therefore, the EFS is bounded and elliptical, which is essentially the same as a dielectric [see Fig. 2(a1)], except that the degeneracy between different polarizations is lifted. All eigenfrequencies are real and the same at $\pm\boldsymbol{k}$. The eigenmodes with nonzero eigenfrequencies satisfy $(\boldsymbol{E}_{\boldsymbol{k}}, \boldsymbol{H}_{\boldsymbol{k}})_j = e^{i\theta_j}(-\boldsymbol{E}^*_{-\boldsymbol{k}}, \boldsymbol{H}^*_{-\boldsymbol{k}})_j$, demonstrating the $\mathcal{CP}$-symmetric phase (see Appendix B for an analytical example).

At the exceptional point $\gamma_z^c = \sqrt{\epsilon_D\mu_D}$, $f_+(\gamma_z)$ diverges, and the Hamiltonian $H(\boldsymbol{k})$ is ill defined because $\det(H_M) = 0$. There are only two solutions for $f_-(\gamma_z)$ with $k_z = \pm\sqrt{-k_t^2/2 + \omega^2\epsilon_D\mu_D}$. The non-Hermitian Hamiltonian $H(\boldsymbol{k})$ is defective at the exceptional point in the sense that the number of linearly independent eigenmodes is less than the dimension of the Hamiltonian, which is different from the defectiveness of $\mathcal{PT}$-symmetric Hamiltonians at the exceptional point that have coalesced eigenstates (i.e., linearly dependent).

Beyond the exceptional point $\gamma_z > \gamma_z^c$, two purely imaginary eigenmodes appear, which denotes the $\mathcal{CP}$-broken regime. Meanwhile, $f_+(\gamma_z)$ becomes positive, leading to the indefinite (hyperbolic) bands [52] [as shown in Fig. 2(a2)], which are similar to type-I HMMs. In Fig. 2(b), we plot the complex band structures at a finite k_z across the $\mathcal{CP}$-breaking transition. Before the transition $\gamma_z < \gamma_z^c$, the degenerate bands (green and red) at $\gamma_z = 0$ split but remain real in the entire momentum space. The purple plane represents static solutions of Maxwell's equations, which are zero for any chiral term. With increasing γ_z, the green band's cone becomes sharper. Across the exceptional point γ_z^c, the real part of the green band first disappears at infinity and then reemerges as the new lower band, which manifests as a cone located at the origin with a quadratic band touching the new upper red band, while the remaining parts become purely imaginary (see Sec. II C for more discussions of the topological nature of this transition). Such band dispersion exhibits an exceptional ring on the k_x-k_y plane [an exceptional cone in three-dimensional (3D) momentum space], where the eigenmodes coalesce to zero eigenfrequency and a null eigenvector.

The existence of multiple chiral terms along different directions provides a tunable tool for driving the $\mathcal{CP}$-breaking transition and engineering different hyperbolic band dispersions. In the case $\gamma = \mathrm{diag}(\gamma_x, \gamma_y, \gamma_z)$, there exist three individual exceptional points at $\gamma_l^c = \sqrt{\epsilon_D \mu_D}$, $l = x, y, z$ along each spatial direction. When all $\gamma_l < \sqrt{\epsilon_D \mu_D}$, the system remains $\mathcal{CP}$ symmetric and has ellipsoid EFSs. When one chiral term such as γ_z exceeds γ_z^c, the system enters the $\mathcal{CP}$-broken phase and exhibits hyperbolic dispersion, as shown in Figs. 2(a2) and 2(b). When γ_y also exceeds the exceptional point, the hyperbolic dispersion changes from type I to type II [see Fig. 2(a3)], and the conelike EFSs lie along the k_x direction, which is perpendicular to the k_z-k_y plane. Interestingly, when all three chiral components exceeds γ_l^c, the system transitions back to the $\mathcal{CP}$-symmetric phase, and the hyperbolic dispersions disappear. This feature is unique to $\mathcal{CP}$-symmetric systems because one always ends up in the $\mathcal{PT}$-broken regime with increasing material gain-loss strength in $\mathcal{PT}$-symmetric systems. More exotic hyperbolic band dispersions, which cannot be realized in metal-dielectric-patterned HMMs, can be engineered through $\mathcal{CP}$ breaking when nondiagonal chiral terms are involved, as shown in two examples illustrated in Figs. 2(a4) and 2(a5). More details on the $\mathcal{CP}$-breaking-induced hyperbolicity are presented in Appendix C. These results clearly show that strong chiral materials may provide a tunable platform for realizing lossless hyperbolic materials and significantly broadening the applications of HMMs.

C. Non-Hermitian topological phase transition

Non-Hermitian effects can bring novel properties to topological systems. The topological bands are generally complex in non-Hermitian photonics, leading to various types of gaps such as point and line gaps [53]. In Hermitian topological photonics, the band-touching points are typically Dirac points or Weyl points [54], while more exotic phenomena such as exceptional points [55] or Weyl exceptional rings [56] can occur in non-Hermitian topological photonics. Moreover, it has been shown that purely non-Hermitian effects like gain and loss can drive nontrivial topological phase transitions in photonics [57–59]. Finally, due to the relaxation of the Hermiticity, non-Hermitian systems enjoy broader symmetry classes, enriching the 10-fold topological classification to a 38-fold classification [60]. Correspondingly, the topological characterization and topological invariants of non-Hermitian photonics can be different, many of which are still under investigation.

While the $\mathcal{PT}$-breaking transition generally does not accompany the change in topological invariants, the $\mathcal{CP}$-breaking transition represents a non-Hermitian topological phase transition in continuous media with interesting properties. In the following, we illustrate such a unique topological phase transition using anisotropic nonmagnetic dielectric media with only nonzero γ_z.

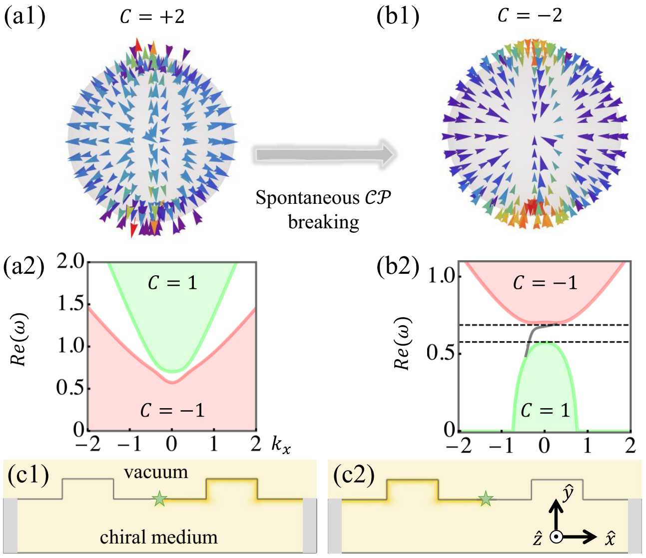

FIG. 3. Non-Hermitian topological photonics through $\mathcal{CP}$ breaking. (a1) Topological charge distribution of the photonic TDP at the origin of momentum space and (a2) the corresponding 2D band structure at $k_z = 1$ with the open boundary condition along y in the $\mathcal{CP}$ -symmetric phase. (b) Similar to (a), but for the $\mathcal{CP}$-broken phase. In (b2), two dashed lines give the photonic band gap of 0.58 to 0.69, and the dark gray curve represents the chiral surface wave. COMSOL MULTIPHYSICS full-wave simulations for edge modes with (c1) $k_z = 1$ and (c2) $k_z = -1$. The green star denotes the location of a line source, and the corresponding input energy is $\omega = 0.59$. The gray-shaded areas represent perfect absorption materials. For all panels, we assume nonmagnetic material $\mu = 1$ and anisotropic dielectric permittivity $\epsilon = (3, 2, 1)$. For the $\mathcal{CP}$-symmetric phase, we take $\gamma_z = 0.5$, while $\gamma_z = 2$ in the broken region.

The topological properties of this continuous system can be understood as a topological semimetal with, instead of Weyl points, photonic triply degenerate points (TDPs) [34,61]. The TDP locates at the origin of momentum space $\boldsymbol{k} = 0$ (see Appendix D for more details) due to the lack of high-symmetry points without lattice symmetries. The topological charge of the TDP can be described by a non-Hermitian Chern number,

$$\mathbf{C}^{ab} = \frac{1}{2\pi} \oint_{S^2} d\mathbf{k} \cdot \nabla \times \mathcal{A}^{ab}, \tag{4}$$

on a two-dimensional (2D) sphere S^2 containing the TDP. The Berry connection $\mathcal{A}^{ab} = -i_a \langle \psi | \partial_{\mathbf{k}} \psi \rangle_b$ and $a, b = L, R$ are used to define left and right eigenvectors $H(\boldsymbol{k})|\psi(\boldsymbol{k})\rangle_R = \omega(\boldsymbol{k})|\psi(\boldsymbol{k})\rangle_R$, and $H^\dagger(\boldsymbol{k})|\psi(\boldsymbol{k})\rangle_L = \omega^*(\boldsymbol{k})|\psi(\boldsymbol{k})\rangle_L$. The fact that the Chern number is gauge independent leads to $C = C^{ab}$ [62].

In the $\mathcal{CP}$-symmetric region, the charge of TDP is found to be $+2$ [34,61], and the distribution of the Berry curvature A^{RR} on a sphere is plotted in Fig. 3(a1). Figure 3(a2) shows the real band structure on a cylindrical geometry with open and periodic boundary conditions along y and x at $k_z = 1$. Such a band structure can be understood from Fig. 2(b), where the anisotropy splits the quadratic band touching at

$(k_x, k_y) = (0, 0)$ into two Dirac points at finite k_x. A finite γ_z breaks the Dirac point, so that the TDP is isolated in the entire momentum space. Once we take an open boundary along y, the bands are projected onto k_x, leading to Fig. 3(a2). In this phase, there is no full gap for any frequency, and the projected band looks similar along k_y or k_z.

In the $\mathcal{CP}$-broken region, the TDP remains, but its topological charge becomes -2 [see Fig. 3(b1)], indicating a topological phase transition associated with the $\mathcal{CP}$ breaking. In the projected bands shown in Fig. 3(b2), there is a full photonic gap, labeled by the dashed lines. To investigate the band topology in two dimensions, we compute the Chern number of each band following the definition in Eq. (4) with S^2 replaced by $\mathbb{R}^2$, which is the 2D infinite plane at any finite k_z (see Appendix D for more details). The band Chern number is found to be nontrivial, as labeled in Figs. 3(a2) and 3(b2). The anisotropic dielectric permittivity plays an important role here as it breaks the degeneracy at $k_x = 0$ and $k_y = 0$ [see Fig. 2(b)].

To explore the bulk-edge correspondence, we solve the surface state as a Dyakonov wave, which is plotted in Fig. 3(b2) as a dark gray curve. We find that the edge modes are all real, which indicates that the edge modes respect $\mathcal{CP}$ symmetry even though the symmetry is spontaneously broken in the bulk. The existence of the chiral edge state is further confirmed by the COMSOL MULTIPHYSICS simulation shown in Fig. 3(c1). The simulation also indicates that the edge modes have only real energy since there are no attenuations or amplifications when they propagate along the edges until they hit the absorption materials on the sides (gray-shaded area).

The above discussion focuses on $k_z > 0$. For $k_z < 0$, the upper-band Chern number in Fig. 3(b2) changes to $+1$, and the total change of -2 when k_z crosses zero represents the topological charge of the TDP at $\boldsymbol{k} = 0$. The reverse of the chiral edge mode at $k_z < 0$ is confirmed by the full-wave simulation shown in Fig. 3(c2), which is a result of breaking $\mathcal{P}$ symmetry.

Generally, topological phase transitions in lattices are accompanied by band gap closing and reopening. In our continuous media, the band Chern number seems to be "exchanged," and the topological charge of the TDP correspondingly reverses after the topological phase transition [see Figs. 3(a) and 3(b)]. However, there is no band gap closing when γ_z is tuned across γ_z^c, as shown in Fig. 4.

When $\gamma_z \to \gamma_z^{c-}$, the green band becomes infinite everywhere, except at $(k_x, k_y) = (0, 0)$ in a 2D plane defined by any finite k_z, which is shown as a sharp cone in Fig. 4(a). At the critical point, Eq. (1) is ill defined as H_M is irreversible, leading to such divergent eigenfrequencies. When $\gamma_z \to \gamma_z^{c+}$, the green band also merges as a sharp cone, but from the zero-real-energy plane [Fig. 4(b)], with the imaginary band approaching infinity. Across the transition, the red band remains real, finite, and continuous. While Eq. (1) cannot be solved directly at $\gamma_z = \gamma_z^c$, the eigenfrequencies at $(k_x, k_y) = (0, 0)$ can be defined by solving both the left and right limits, which are equivalent to each other. Therefore, the gap between the green and red bands can be defined in the entire 2D plane, which remains finite and open throughout the topological phase transition.

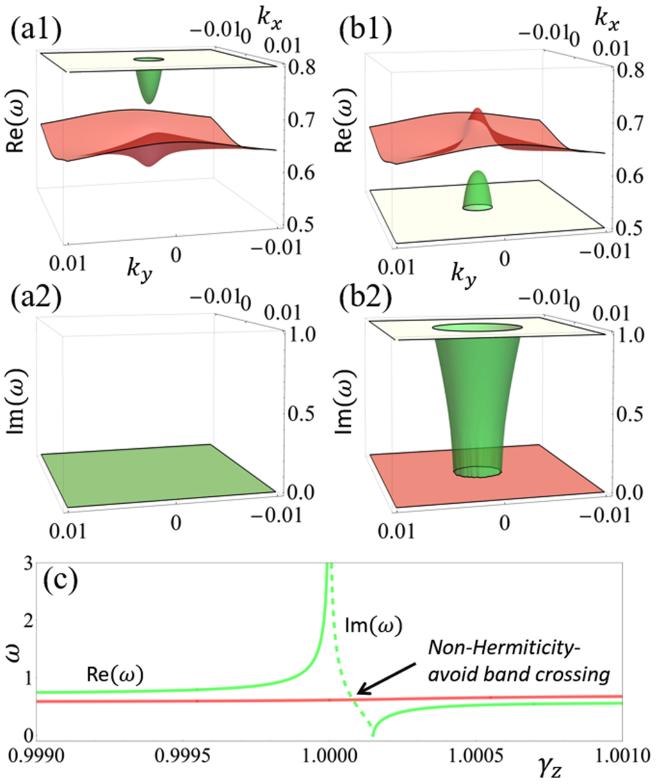

FIG. 4. Band exchange at infinity. (a) Band structure near the origin on the $k_z = 1$ plane in the $\mathcal{CP}$-symmetric region when $\gamma_z \to \gamma_z^{c-}$. (b) Similar to (a), but plotted in the $\mathcal{CP}$-broken region with $\gamma_z \to \gamma_z^{c+}$. (c) Evolution of two bands with respect to γ_z across the critical point near the origin of the $k_z = 1$ plane. Note that only nonzero imaginary (dashed curves) and real (solid curves) parts are plotted for better visualization.

In Fig. 4(c), we plot the bands at $k_x, k_y \ll 1$ with respect to varying γ_z near the vicinity of γ_z^c. Clearly, the green band connects to infinite real energy and zero imaginary energy at the critical point and then comes back from infinite imaginary energy and zero real energy. That is, the green band travels from higher energy to lower energy by making itself purely imaginary, which reverses the band topology without crossing the real red band. Such a *non-Hermitian avoided band crossing* is unique to non-Hermitian systems and implies more fundamental and distinctive topological properties of open systems.

III. APPLICATIONS OF NON-HERMITIAN PHOTONICS BASED ON $\mathcal{CP}$ SYMMETRY

Besides the distinct non-Hermitian topological phase transition without gap closing, the non-Hermitian photonics based on $\mathcal{CP}$ symmetry may have potential applications in a plethora of fields due to the rise of hyperbolicity. For example, hyperbolic bands can be utilized to fabricate superresolution lenses [29,63], superresolution photolithography [64], high-sensitivity sensors [30], and ultrafast lasers or light-emitting diodes [65]. In the following, we illustrate their two important device applications in classical optical devices and laser engineering.

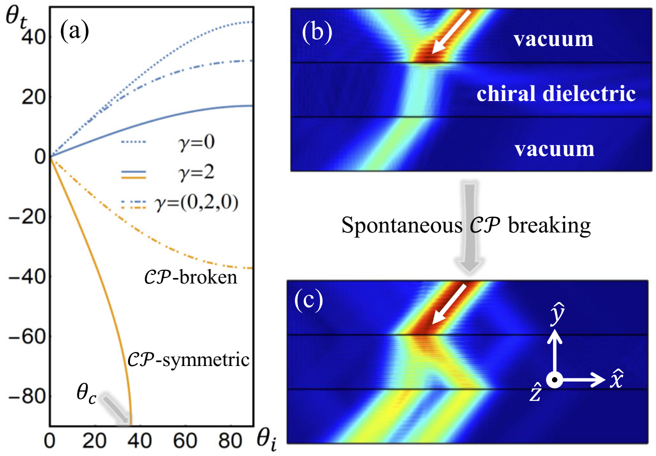

FIG. 5. All-angle and polarization-dependent negative refraction. (a) Analytic calculations of a linearly polarized plane wave transmitting on the boundary between a chiral dielectric and a vacuum. The plot shows transmitted angle θ_t with respect to different incident angles θ_i. The blue and yellow curves represent right-handed and left-handed polarizations. (b) and (c) COMSOL MULTIPHYSICS simulations for (a). The incident angle is fixed at $\theta_i = 40^\circ$, while $\gamma = 2I_3$ and $\gamma = \text{diag}(0, 2, 0)$ for (b) and (c), respectively. The white arrows denote the incident directions.

A. All-angle polarization-dependent beam splitter

For practical device applications, it is desirable to be able to control the constituent materials' optical properties. This can be achieved by material engineering, thermal tuning, and nonequilibrium modulation, to name a few methods [66–70].

Birefringence and negative refraction have long been studied in chiral media, and it is known that there is a critical angle θ_c, beyond which one polarization is totally reflected [50]. The critical angle vanishes in $\mathcal{CP}$-broken regimes because the negative refraction has been promoted to an all-angle effect thanks to indefinite bands. This is demonstrated by the analytic results [Fig. 5(a)], together with the COMSOL MULTIPHYSICS simulation [Figs. 5(b) and 5(c)]. Because of the polarization dependence of the chiral media shown in Fig. 5(a), the $\mathcal{CP}$-symmetric photonics promises an all-angle polarization-dependent beam splitter, a device that is hard to engineer in either HMM or $\mathcal{CP}$-symmetric dielectrics.

The details of analytic and numeric calculations are discussed in Appendix E.

B. Enhanced spontaneous emissions for laser engineering

Spontaneous emissions play a crucial role for laser engineering and have been widely studied in chiral media, but mainly in the $\mathcal{CP}$-symmetric regime. The hyperbolic bands in the $\mathcal{CP}$-broken regime can significantly enhance the spontaneous emissions of a dielectric continuum with both broader bandwidth and a stronger Purcell effect [23].

Through Fermi's golden rule, we can easily see that the radiative decay rate is generally proportional to the photonic density of states $\rho(\omega) = \sum_{\sigma,\boldsymbol{k}} \delta(\omega_{\sigma,\boldsymbol{k}} - \omega)$, where the summation goes over all polarizations σ and momenta $\boldsymbol{k}$. The density of states is proportional to the area of EFSs at $\omega_{\sigma,\boldsymbol{k}} = \omega$, which is a small finite value for dielectrics but diverges for HMMs. Note that it does not diverge in real physical systems due to finite-size effects and corrections of effective-medium theory for large $\boldsymbol{k}$ states [20]. Based on the above arguments, a hyperbolic dispersion would render a larger radiative decay rate and thus a stronger Purcell effect. The Purcell effect characterizes the enhancement or inhibition of spontaneous emission in a system with respect to free space. For most nanophotonic applications, a stronger Purcell effect (i.e., a larger Purcell factor) is desired.

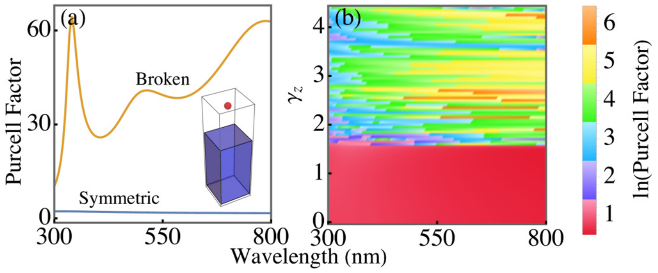

FIG. 6. Spontaneous emissions enhanced by $\mathcal{CP}$ breaking. (a) Isotropic Purcell factor for a bulk SiO_2 crystal with chiral effects $\gamma = (0, 0, 1)$ ($\mathcal{CP}$ symmetric) and $\gamma = (0, 0, 2)$ ($\mathcal{CP}$ broken). The inset shows the setup, where the cuboid represents the dielectric, and the red sphere is a dipolar source. (b) Phase diagram of the Purcell factor in logarithmic scale. The setup is the same as in the inset in (a).

With the physical understanding, we expect to observe a jump in the Purcell factor in the chiral medium at a given wavelength upon crossing the exceptional point and entering the $\mathcal{CP}$-broken region. This is further confirmed by the COMSOL MULTIPHYSICS simulations shown in Fig. 6. We consider a SiO_2 crystal sample with size $100 \times 100 \times 200$ nm^3. An electric dipole source in vacuum is placed 10 nm above the sample in the x-y plane [see the inset in Fig. 6(a)], and the plotted Purcell factor is averaged through three dipolar configurations along three spatial directions [24].

For simplicity, we consider only a wavelength-independent chiral term along the z direction, which renders, in the $\mathcal{CP}$-broken region, indefinite bands similar to Fig. 2(a2). Two examples with $\gamma_z = 1$ and $\gamma_z = 2$ are plotted in Fig. 6(a), corresponding to the symmetric and broken phases, respectively. The latter shows a very strong Purcell effect with a sharp peak around 320 nm, and the broadband enhancement is observed on the right-hand side (long wavelength). We further scan the phase diagram of the Purcell factor and plot it in Fig. 6(b). The sharp boundary around $\gamma_z \approx 1.55$ manifests the $\mathcal{CP}$-breaking critical point, at which a large leap of the Purcell factor is observed. Note that the boundary is not exact at different wavelengths as the actual reflective index of SiO_2 varies. Our simulation also indicates that the Purcell factor could reach the order of $e^6 \approx 400$ in proper regions. Therefore, such a chiral dielectric material provides an ideal platform for engineering topological lasers with edge-mode lasing and enhanced spontaneous emission.

IV. CONCLUSION AND DISCUSSION

In the current literature, chirality can be obtained either from chiral molecules [37] or from certain spatially spiral nanostructures, i.e., chiral metamaterials [42]. Therefore, the proposed chiral dielectric materials can be realized by creating chiral metamaterials with nanofabrication considerations in mind and can be characterized by measuring the circular dichroism spectra [71]. Alternatively, dielectric chiral molecules can be utilized, with the material hyperbolicity directly characterized by the Muller matrix ellipsometry [72]. If chiral dielectrics with optical gain are used, the topological edge modes can be promoted to lasing edge modes and can be measured using standard microphotoluminescence techniques [73].

Since the dielectric material with chirality shows hyperbolic dispersion, it exhibits a higher optical density of states than its surrounding material. Thus, insertion loss is unavoidable when the high-momentum components outcouple from the chiral dielectric material to its surroundings. Two suitable approaches that have been reported to minimize the insertion loss are dispersion engineering [74] and the addition of a grating coupler [75]. For our proposed chiral dielectric material, adding a subwavelength grating is an option as it can be fabricated on the material via focused ion-beam milling [75].

In terms of the operation bandwidth of the proposed chiral dielectric, we can design the chiral metamaterials on a scale similar to the wavelength to target different frequency ranges from optical to microwave frequencies [76].

In conclusion, we proposed a class of non-Hermitian topological photonics based on $\mathcal{CP}$ symmetry which is dramatically different from the well-known $\mathcal{PT}$-symmetric photonics. The physical realization of such $\mathcal{CP}$-symmetric photonics in chiral dielectrics opens a pathway for engineering exotic lossless hyperbolic materials with significant applications. Importantly, we revealed a class of non-Hermitian topological phase transition in continuous media without band gap closing. Our work may shed light on future experimental and theoretical development of new non-Hermitian photonics.

Many important questions remain to be answered for the $\mathcal{CP}$-symmetric non-Hermitian photonics, and here we list a few of them: (i) Can $\mathcal{CP}$ symmetry and its breaking be induced by means other than chiral effects? (2) Can $\mathcal{CP}$-symmetric photonics be applied to periodic optical systems like photonic crystals or coupled optical cavities? (iii) Are there other paths to non-Hermitian photonics besides $\mathcal{PT}$ and $\mathcal{CP}$ symmetries? (iv) Finally, does such $\mathcal{CP}$-symmetric non-Hermitian physics exist in physical systems other than photonics?

ACKNOWLEDGMENTS

This work was supported by the Air Force Office of Scientific Research (Grant No. FA9550-20-1-0220), the National Science Foundation (Grants No. PHY-1806227, No. PHY-2110212), the Army Research Office (Grant No. W911NF-17-1-0128), and UT Dallas Office of Research through the SPIRe Grant Program. Z.L. and Q.G. acknowledge funding from the Welch Foundation (Grant No. AT-1992-20190330) and UT Dallas faculty startup funding.

APPENDIX A: DIAGNOSIS OF A SIMPLE $\mathcal{PT}$ MODEL

A simple model for $\mathcal{PT}$ photonics is

$$H_{PT} = t\sigma_x + i\gamma_g\sigma_z, \quad t \in \mathbb{R}, \quad \gamma_g \in \mathbb{R}, \tag{A1}$$

which describes a one-dimensional coupled microcavity array with patterned gain and loss γ_g. The hopping coefficient t is assumed to be real, and the spectrum with $t = 1$ is plotted in Fig. 1(a).

For such a system, we could define the symmetry operators $\mathcal{P} = \sigma_x$ and $\mathcal{T} = K$. The eigenmodes, in both symmetric and broken phases, are related in a way similar to what we discussed in Sec. II A . Specifically, in the symmetric phase, we have $\psi_j = e^{i\theta_j}(\mathcal{PT})\psi_j$, followed by the real spectrum $\omega_j = \omega_j^*$, where the eigenmodes are defined as $H_{PT}\psi_j = \omega_j\psi_j$, $j = 0, 1$. In the broken regime, the two eigenmodes are related as $\psi_j = e^{i\theta_j}(\mathcal{PT})\psi_{\bar{j}}$, so that the spectrum is a complex conjugate pair $\omega_j = \omega_{\bar{j}}^*$ and $\bar{j} = 1 - j$.

APPENDIX B: EXAMPLE OF $\mathcal{CP}$ BREAKING

In the main text, we argued that the spontaneous breaking of $\mathcal{CP}$ symmetry may lead to complex eigenmodes, which can be understood through the transformation of eigenmodes at $\pm\boldsymbol{k}$. If $(\mathcal{CP})\psi_{j,\boldsymbol{k}} = e^{i\theta_j}\psi_{j,-\boldsymbol{k}}$, there is a constraint on eigenfrequencies $\omega_{j,\boldsymbol{k}} = \omega_{j,-\boldsymbol{k}}^*$, which dictates a real spectrum. Here we show an example in both $\mathcal{CP}$-symmetric and $\mathcal{CP}$-broken regions by writing down the eigenmodes explicitly. We take $\epsilon_D = 4$, $\mu_D = 1$, $\gamma = \mathrm{diag}(0, 0, \gamma_z)$, and $\boldsymbol{k} = (k_x, k_y, k_z) = (1, 1, 1)$. The exceptional point is then $\gamma_z^c = 2$.

There are two nonzero and positive (in the $\mathcal{CP}$-symmetric regime) solutions, $\omega_{0,\pm\boldsymbol{k}} = (6 - \gamma_z)/(2\gamma_{z,-})$ and $\omega_{1,\pm\boldsymbol{k}} = (6 + \gamma_z)/(2\gamma_{z,+})$, with eigenstates (we can take only either the positive or negative branches for a given system)

$$\psi_{0,\pm\boldsymbol{k}} = \left(\frac{i(2-\gamma_z) \pm \gamma_{z,-}}{8}, \frac{i(2-\gamma_z) \mp \gamma_{z,-}}{8}, -\frac{i}{2}, \frac{\gamma_z - 2 \pm i\gamma_{z,-}}{4}, \frac{\gamma_z - 2 \mp i\gamma_{z,-}}{4}, 1\right)^T, \tag{B1}$$

$$\psi_{1,\pm\boldsymbol{k}} = \left(-\frac{i(\gamma_z+2) \pm \gamma_{z,+}}{8}, -\frac{i(\gamma_z+2) \mp \gamma_{z,+}}{8}, \frac{i}{2}, -\frac{\gamma_z + 2 \mp i\gamma_{z,+}}{4}, -\frac{\gamma_z + 2 \pm i\gamma_{z,+}}{4}, 1\right)^T, \tag{B2}$$

where $\gamma_{z,\pm} = \sqrt{(\gamma_z \pm 6)(\gamma_z \pm 2)}$.

When $0 < \gamma_z < \gamma_z^c$, $\gamma_{z,\pm} > 0$. It is obvious that $(\mathcal{CP})\psi_{j,\boldsymbol{k}} = e^{i\pi}\psi_{j,-\boldsymbol{k}}$, such that $\omega_{j,\boldsymbol{k}} = \omega_{j,\boldsymbol{k}}^*$, which is in the $\mathcal{CP}$-symmetric phase. When $\gamma_z > \gamma_z^c$, $\gamma_{z,+} > 0$, but $\gamma_{z,-}$ becomes purely imaginary. The condition $(\mathcal{CP})\psi_{1,\boldsymbol{k}} = e^{i\pi}\psi_{1,-\boldsymbol{k}}$ survives, so there is still one real eigenmode. The transformation for the other one becomes $(\mathcal{CP})\psi_{1,\pm\boldsymbol{k}} = e^{i\pi}\psi_{1,\pm\boldsymbol{k}}$, which requires $\omega_{1,\pm\boldsymbol{k}} = -\omega_{1,\pm\boldsymbol{k}}^*$. The $\mathcal{CP}$ symmetry is partially broken by strong chiral effects, and the eigenspectra become complex.

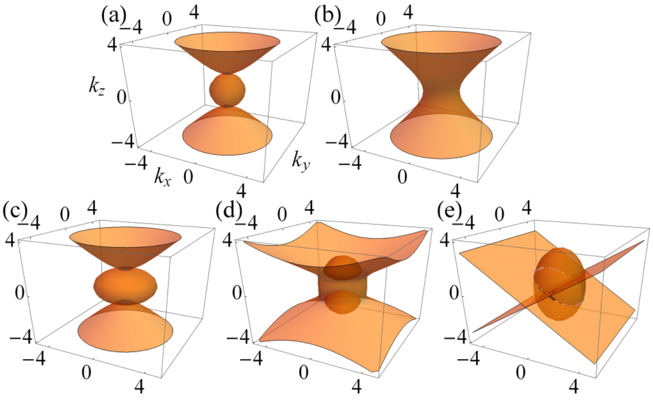

FIG. 7. Hyperbolic dispersions in HMMs and $\mathcal{CP}$-broken dielectrics. Typical EFSs at $\omega = 1$ for (a) type-I and (b) type-II HMMs. We choose $\epsilon = \mathrm{diag}(2, 2, -2)$ and $\epsilon = \mathrm{diag}(-2, -2, 2)$, respectively. Corresponding realizations of dispersion relations in strong chiral dielectrics for (c) $\epsilon = 2I_3$, $\gamma = \mathrm{diag}(0, 0, 3)$, (d) $\epsilon = \mathrm{diag}(1, 1, 2)$, $\gamma = \mathrm{diag}(1.5, 1.5, 0)$, and (e) $\epsilon = \mathrm{diag}(2, 2, 2)$, $\gamma = \mathrm{diag}(2, \sqrt{2}, 0)$. For all panels $\mu = I_3$.

APPENDIX C: HYPERBOLIC BANDS FROM $\mathcal{CP}$ BREAKING BY CHIRAL EFFECTS

The EFSs for pure dielectric materials are spheres (ellipsoids) in the momentum space. However, the EFSs for HMMs are completely different, as shown in Figs. 7(a) and 7(b), corresponding to type-I and type-II HMMs, respectively [19,20]. A significant feature of these EFSs is that they stretch to infinity in momentum space, so that the material can support the propagation of large $|\mathbf{k}|$ waves. Such hyperbolicity was thought to be unique to HMMs [20]. Quite surprisingly, similar dispersions can also be realized through $\mathcal{CP}$ breaking induced by chiral terms. The corresponding EFSs are plotted in Figs. 7(c) and 7(d).

As observed in Fig. 7(c), the chiral term along one spatial direction exceeding the exceptional point can render a dispersion relation mimicking that of a type-I HMM. If the chiral terms along two spatial directions exceed the exceptional points, the dispersion relation is similar to that for a type-II HMM, as shown in Fig. 7(d). Nevertheless, the geometries are not exactly the same in the small-$|\mathbf{k}|$ region because we have two bounded EFSs surrounded by the hyperbolic one. While we presented similar results and some exotic hyperbolic dispersions in the main text, Fig. 7(e) offers an example where the system is $\mathcal{CP}$ broken in one direction and at the exceptional point in another direction.

In the following, we study the wave propagation in chiral media and show how the hyperbolic dispersions emerge. We first consider a chiral isotropic dielectric medium with constant scalar permittivity, permeability, and chiral effect $\gamma = \gamma_D I_3$, as defined in the main text. This simple model is enough to gain insights into the systems and has been adopted frequently in previous studies [41,48–50]. The resulting dispersion relation is

$$\omega = |\mathbf{k}|/|\sqrt{\epsilon_D\mu_D} \pm \gamma_D|. \tag{C1}$$

For $\gamma_D = 0$, the EFS is a twofold-degenerate sphere, as expected, and the degeneracy comes from two different polarizations. For a finite chiral strength, the degeneracy is lifted, and there are always two spheres with different radii in the momentum space except at $\gamma_D = \pm\sqrt{\epsilon_D\mu_D}$. It has been shown that for $|\gamma_D| > \sqrt{\epsilon_D\mu_D}$, there is negative refraction for proper incident angles because the time-averaged Poynting vector $\langle \mathbf{S}\rangle_t$ is antiparallel to $\mathbf{k}$ [50]. This result is straightforward if we notice that the refraction indexes are $n = \sqrt{\epsilon_D\mu_D} \pm \gamma_D$ for right- and left-handed circular polarizations [43]. Nevertheless, the EFSs always remain ellipsoids for both $\gamma_D < \sqrt{\epsilon_D\mu_D}$ and $\gamma_D > \sqrt{\epsilon_D\mu_D}$ as a result of linear dispersion relations. Due to the bounded EFSs, there exists a critical angle θ_c in a scalar chiral medium, beyond which the incident waves with certain polarizations are totally reflected. A scalar chiral term cannot render spontaneous $\mathcal{CP}$ breaking, which requires strong anisotropic chiral terms.

We now revisit the simple, but instructive, case in the main text with slightly different $\epsilon = \mathrm{diag}(\epsilon_t > 0, \epsilon_t > 0, \epsilon_z > 0)$, $\mu = 1$, and $\gamma = \mathrm{diag}(0, 0, \gamma_z)$. The dispersion relation becomes

$$\left(k_t^2 + k_z^2 - \epsilon_t\omega^2\right)\left(\epsilon_t k_t^2 + \epsilon_z k_z^2 - \epsilon_z\epsilon_t\omega^2\right) = \gamma_z^2\left(k_z^2 - \epsilon_t\omega^2\right)^2, \tag{C2}$$

where $k_t^2 = k_x^2 + k_y^2$. Our previous analysis suggests that there is an exceptional point $\gamma_z = \pm\sqrt{\epsilon_z}$ since γ_z is decoupled from k_x and k_y in Eq. (C2). For a small γ_z, we have two distinguishable ellipsoids since the degeneracies between different polarizations are lifted. As the chiral strength increases, the inner EFS gets compressed along both the k_x and k_y directions and disappears at the exceptional point. After passing the exceptional point, the EFSs are not two ellipsoids anymore because the leading term $(\epsilon_z - \gamma_z^2)\epsilon_t^2\omega^4$ becomes negative, which mimics a type-I HMM. As a result, we observe type-I hyperbolic dispersions in the $\mathcal{CP}$-broken phase since hyperbolic bands must be non-Hermitian due to its metal character. Note that the two degenerate points at $\mathbf{k} = (0, 0, \pm k_z)$ survive but can be lifted by anisotropy in the permeability tensor $\epsilon_x \neq \epsilon_y$ or additional chiral terms.

Although the chirality-induced hyperbolic dispersion has an EFS similar to that for HMMs, it is impossible to obtain a homogeneous model for a strong chiral medium similar to that for a simple HMM. In a chiral medium, eigenmodes with different polarizations are not degenerate. The existence of chiral effects also breaks all spatial inversion symmetries, while a pure HMM preserves them. However, by comparing the wave equations in the frequency-momentum domain, we can recast the chiral medium with only nonzero γ_z into a "pure HMM" form,

$$\epsilon_{\mathrm{eff}} = \left[\epsilon_t, \epsilon_t, \epsilon_z - \gamma_z^2\left(k_z^2 - \epsilon_t\omega^2\right)/\left(k_t^2 + k_z^2 - \epsilon_t\omega^2\right)\right], \tag{C3}$$

where the effective ϵ_{eff} along the z direction depends on k_z and ω. Such a projection cannot be applied to materials with nonvanishing chiral effects along two directions because there are coupled terms like $\gamma_i\gamma_j$, $i \neq j$, which lead to the difference in the geometries of EFSs [see Figs. 7(b) and 7(d)].

Although exceptional points along three spatial directions are decoupled when γ and ϵ (or μ) commute, the situation can be much more complicated if there are nondiagonal terms in the chiral tensor. When there are only diagonal chiral terms, the exceptional points form two intersecting exceptional lines that separate the phase diagram into four parts [Fig. 8(a)].

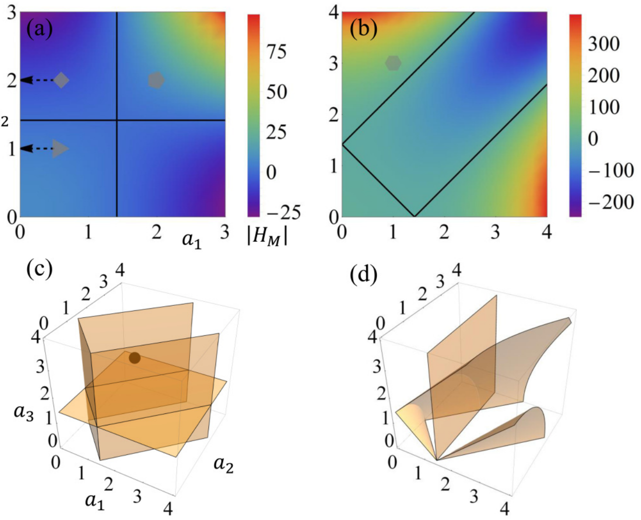

FIG. 8. Phase diagram with different chiral effects. (a) Density plot of det $|H_M|$. The solid black curves denote zero solutions (exceptional points). $\gamma = \mathrm{diag}(0, a1, a2)$. The triangle, square, and pentagon represent the parameters for Figs. 2(a1), 2(a2), and 2(a3), respectively. (b) Similar to (a), but the chiral term is chosen to be $\gamma = \begin{pmatrix} a1 & a2 & 0 \\ a2 & a1 & 0 \\ 0 & 0 & 0 \end{pmatrix}$. The hexagon corresponds to Fig. 2(a4). (c) and (d) Phase boundary for chiral terms $\gamma = \begin{pmatrix} a1 & a2 & 0 \\ a2 & a1 & 0 \\ 0 & 0 & a3 \end{pmatrix}$ and $\gamma = \begin{pmatrix} a1 & a2 & a3 \\ a2 & a1 & 0 \\ a3 & 0 & a1 \end{pmatrix}$. The brown ball gives the parameters used in Fig. 2(a5).

The phase boundary changes when a nondiagonal term is considered [Fig. 8(b)], which is accompanied by some exotic hyperbolic dispersions. In 3D parameter spaces, exceptional surfaces exist [Figs. 8(c) and 8(d)]. We see the complex chiral configurations lead to hyperbolic dispersions that cannot be realized in regular HMMs.

APPENDIX D: PHOTONIC TRIPLY DEGENERATE POINT

In the main text, we discussed the TDP at the origin of momentum space without inspecting the band structure. Here we characterize the band dispersion of both real and complex TDPs in the $\mathcal{CP}$-symmetric and -broken phases.

The real TDP in the $\mathcal{CP}$-symmetric phase is depicted in Figs. 9(a) and 9(b), projected to the $k_x = 0$ and $k_z = 0$ planes, respectively. Both the green and red bands show linear dispersion along all spatial directions, and the bands are gapped everywhere except for the TDP at the origin.

In the $\mathcal{CP}$-broken region, the TDP mimics that studied in a genuine HMM with small chirality terms [34]. The red band is real in the entire momentum space and shows linear dispersions as in the symmetric phase [see Figs. 9(c1) and 9(d1)]. On the contrary, the green band becomes complex in the broken phases. It is either purely real or purely imaginary in the $k_x = 0$ plane [see Fig. 9(c2)], and it is a purely imaginary cone in the $k_z = 0$ plane. The band structure in the $k_y = 0$ plane is similar to Figs. 9(c1) and 9(c2) since the $\mathcal{CP}$ breaking happens only in the z direction. The bands remain gapped everywhere in the momentum space, except at the origin, so that the photonic TDP is well defined.

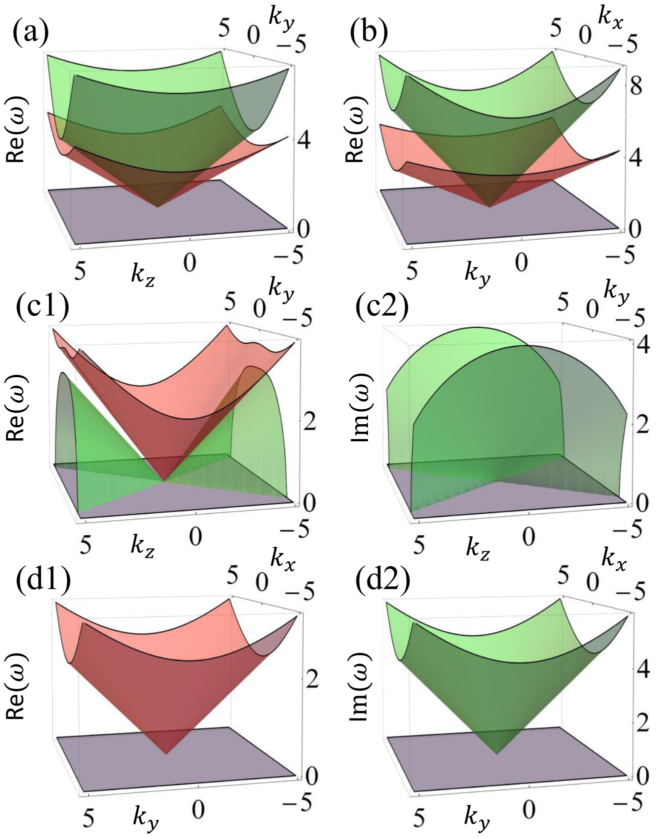

FIG. 9. Real and complex photonic triply degenerate points. Real TDPs in the (a) $k_x = 0$ and (b) $k_z = 0$ planes. The charge distribution is plotted in Fig. 3(a1). (c) and (d) Complex TDPs corresponding to Fig. 3(a2). (c) shows the (c1) real and (c2) imaginary bands in $k_x = 0$, while (d) depicts the band structure in $k_z = 0$.

In the calculation of the 2D band Chern number for a fixed k_z plane, we notice that such a band Chern number defined on an open manifold may not be quantized. However, it has been shown that for continuous media, the base manifold $\mathbb{R}^2$ can be compactified into a sphere S^2, so that the photonic band Chern number is still strictly quantized and gauge invariant [34].

APPENDIX E: ALL-ANGLE POLARIZATION-DEPENDENT BEAM SPLITTER

To compute Fig. 5(a), we choose the x-y plane to be the plane of incidence and the y axis to be the norm, and the incident beam comes from the right side of the norm. The chiral medium locates at $y < 0$, and the region $y \geqslant 0$ is a vacuum. The incident and refraction angles are θ_i and θ_t, respectively. The simulations in Figs. 5(b) and 5(c) are performed in COMSOL MULTIPHYSICS.

As we discussed before, a scalar chiral term could render negative refraction, but only for a small range of the incident angle. This effect is illustrated in Fig. 5(a) by the solid curves. The negatively refracted beam disappears when the incident angle exceeds a critical value, $\theta_c \sim 36^\circ$, which can be attributed to bounded EFSs. As a comparison, we also plot the θ_i-θ_t relation for a pure dielectric, shown by the dashed curve. There is only one single curve due to the lack of the birefringence effect.

Thanks to the hyperbolic dispersion, all-angle negative refraction, which is polarization independent, can be realized in HMMs [21]. In the $\mathcal{CP}$-broken region, the hyperbolic dispersion allows the realization of all-angle polarization-sensitive birefringence and negative refraction. We consider a dielectric with chiral vector $\gamma = \mathrm{diag}(0, 2, 0)$, which is in the $\mathcal{CP}$-broken phase with a type-I hyperbolic dispersion. In Fig. 5(a), we see that the negative refraction indeed happens for arbitrary incident angles. We further confirm these results through COMSOL MULTIPHYSICS simulations, the results of which are plotted in Figs. 5(b) and 5(c). There is no negative refraction when $\theta_i > \theta_c$ in the $\mathcal{CP}$-symmetric phase. This effect can be used to engineer an all-angle polarization beam splitter.

[1] C. M. Bender and S. Boettcher, Real Spectra in Non-Hermitian Hamiltonians Having PT Symmetry, Phys. Rev. Lett. **80**, 5243 (1998).

[2] M. Lax, W. H. Louisell, and W. B. McKnight, From Maxwell to paraxial wave optics, Phys. Rev. A **11**, 1365 (1975).

[3] L. Feng, R. El-Ganainy, and L. Ge, Non-Hermitian photonics based on parity-time symmetry, Nat. Photonics **11**, 752 (2017).

[4] R. El-Ganainy, K. G. Makris, M. Khajavikhan, Z. H. Musslimani, S. Rotter, and D. N. Christodoulides, Non-Hermitian physics and PT symmetry, Nat. Phys. **14**, 11 (2018).

[5] W. D. Heiss, Exceptional points of non-Hermitian operators, J. Phys. A **37**, 2455 (2004).

[6] M. Wimmer, A. Regensburger, M.-A. Miri, C. Bersch, D. N. Christodoulides, and U. Peschel, Observation of optical solitons in PT-symmetric lattices, Nat. Commun. **6**, 7782 (2015).

[7] H. Hodaei, M.-A. Miri, M. Heinrich, D. N. Christodoulides, M. Khajavikhan, Parity-time-symmetric microring lasers, Science **346**, 975 (2018).

[8] J. Zhang *et al.*, A phonon laser operating at an exceptional point, Nat. Photonics **12**, 479 (2018).

[9] Z. Lin, H. Ramezani, T. Eichelkraut, T. Kottos, H. Cao, and D. N. Christodoulides, Unidirectional Invisibility Induced by $\mathcal{PT}$-Symmetric Periodic Structures, Phys. Rev. Lett. **106**, 213901 (2011).

[10] W. Chen, J. Zhang, B. Peng, S. K. Özdemir, X. Fan, and L. Yang, Parity-time-symmetric whispering-gallery mode nanoparticle sensor, Photonics Res. **6**, A23 (2018).

[11] S. Weimann *et al.*, Topologically protected bound states in photonic parity-time-symmetric crystals, Nat. Mater. **16**, 433 (2017).

[12] M. Pan, H. Zhao, P. Miao, S. Longhi, and L. Feng, Photonic zero mode in a non-Hermitian photonic lattice, Nat. Commun. **9**, 1308 (2018).

[13] A. V. ZayatsaIgor, I. Smolyaninovb, and A. A. Maradudinc, Nano-optics of surface plasmon polaritons, Phys. Rep. **408**, 131 (2005).

[14] J. M. Pitarke, V. M. Silkin, E. V. Chulkov, and P. M. Echenique, Theory of surface plasmons and surface-plasmon polaritons, Rep. Prog. Phys. **70**, 1 (2007).

[15] M. Silveirinha and N. Engheta, Tunneling of Electromagnetic Energy through Subwavelength Channels and Bends Using ϵ-Near-Zero Materials, Phys. Rev. Lett. **97**, 157403 (2006).

[16] B. Edwards, A. Alu, M.E. Young, M. Silveirinha, and N. Engheta, Experimental Verification of Epsilon-Near-Zero Metamaterial Coupling and Energy Squeezing Using a Microwave Waveguide, Phys. Rev. Lett. **100**, 033903 (2008).

[17] R. Maas, J. Parsons, N. Engheta, and A. Polman, Experimental realization of an epsilon-near-zero metamaterial at visible wavelengths, Nat. Photonics **7**, 907 (2013).

[18] S. A. R. Horsley and M. Woolley, Zero-refractive-index materials and topological photonics, Nat. Phys. **17**, 348 (2021).

[19] D. R. Smith and D. Schurig, Electromagnetic Wave Propagation in Media with Indefinite Permittivity and Permeability Tensors, Phys. Rev. Lett. **90**, 077405 (2003).

[20] A. Poddubny, I. Iorsh, P. Belov, and Y. Kivshar, Hyperbolic metamaterials, Nat. Photonics **7**, 948 (2013).

[21] Y. Liu, G. Bartal, and X. Zhang, All-angle negative refraction and imaging in a bulk medium made of metallic nanowires in the visible region, Opt. Express **16**, 15439 (2008).

[22] M. Shoaei, M. Kazem Moravvej-Farshi, and L. Yousefi, All-optical switching of nonlinear hyperbolic metamaterials in visible and near-infrared regions, J. Opt. Soc. Am. B **32**, 2358 (2015).

[23] L. Ferrari, D. Lu, D. Lepage, and Z. Liu, Enhanced spontaneous emission inside hyperbolic metamaterials, Opt. Express **22**, 4301 (2014).

[24] D. Lu, J. J. Kan, E. E. Fullerton, and Z. Liu, Enhancing spontaneous emission rates of molecules using nanopatterned multilayer hyperbolic metamaterials, Nat. Nanotechnol. **9**, 48 (2014).

[25] L. Ferrari, J. S. T. Smalley, Y. Fainman, and Z. Liu, Hyperbolic metamaterials for dispersion-assisted directional light emission, Nanoscale **9**, 9034 (2014).

[26] T. Galfsky, Z. Sun, C. R. Considine, C. T. Chou, W. C. Ko, Y. H. Lee, E. E. Narimanov, and V. M. Menon, Broadband Enhancement of Spontaneous Emission in Two-Dimensional Semiconductors Using Photonic Hypercrystals, Nano Lett. **16**, 4940 (2016).

[27] R. Chandrasekar *et al.*, Lasing Action with Gold Nanorod Hyperbolic Metamaterials, ACS Photonics **4**, 674 (2017).

[28] Z. Jacob, L. V. Alekseyev, and E. Narimanov, Optical Hyperlens: Far-field imaging beyond the diffraction limit, Opt. Express **14**, 8247 (2006).

[29] Z. Liu, H. Lee, Y. Xiong, C. Sun, and X. Zhang, Far-field optical hyperlens magnifying sub-diffraction-limited objects, Science **315**, 1686 (2007).

[30] A. V. Kabashin *et al.*, Plasmonic nanorod metamaterials for biosensing, Nat. Mater. **8**, 867 (2009).

[31] Y. Xiang, X. Dai, J. Guo, H. Zhang, S. Wen, and D. Tang, Critical coupling with graphene-based hyperbolic metamaterials, Sci. Rep. **4**, 5483 (2014).

[32] W. Gao, M. Lawrence, B. Yang, F. Liu, F. Fang, B. Beri, J. Li, and S. Zhang, Topological Photonic Phase in Chiral Hyperbolic Metamaterials, Phys. Rev. Lett. **114**, 037402 (2015).

[33] R.-L. Chern and Y. Z. Yu, Chiral surface waves on hyperbolic-gyromagnetic metamaterials, Opt. Express **25**, 11801 (2017).

[34] J. Hou, Z. Li, X.-W. Luo, Q. Gu, C. Zhang, Topological Bands and Triply-Degenerate Points in Non-Hermitian Hyperbolic Metamaterials, Phys. Rev. Lett. **124**, 073603 (2020).

[35] X. Ni *et al.*, Loss-compensated and active hyperbolic metamaterials, Opt. Express **19**, 25242 (2011).

[36] T. Galfsky, H. N. S. Krishnamoorthy, W. Newman, E. E. Narimanov, Z. Jacob, and V. M. Menon, Active hyperbolic metamaterials: Enhanced spontaneous emission and light extraction, Optica **2**, 62 (2015).

[37] A. J. Viitanen, A. Sihvola, I. V Lindell, and S. Tretyakov, *Electromagnetic Waves in Chiral and Bi-isotropic Media* (Artech House, Boston, 1994).

[38] L. Lu, J. D. Joannopoulos, and M. Soljacic, Topological photonics, Nat. Photonics **8**, 821 (2014).

[39] C. Caloz, A. Alu, S. Tretyakov, D. Sounas, K. Achouri, and Z. L. Deck-Leger, Electromagnetic Nonreciprocity, Phys. Rev. Appl. **10**, 047001 (2018).

[40] The $\mathcal{CPT}$ symmetries here are all classical and should not be confused with those in quantum field theory, where $\mathcal{C}$ is always respected by electromagnetism. See, e.g., M. E. Peskin and D. V. Schroeder, *An Introduction to Quantum Field Theory* (CRC Press, Boca Raton, 2018).

[41] J. Lekner, Optical properties of isotropic chiral media, J. Opt. **5**, 417 (1996).

[42] S. S. Oh and O. Hess, Chiral metamaterials: Enhancement and control of optical activity and circular dichroism, Nano Convergence **2**, 24 (2015).

[43] Z. Wang, F. Cheng, T. Winsor, and Y. Liu, Optical chiral metamaterials: A review of the fundamentals, fabrication methods and applications, Nanotechnology **27**, 412001 (2016).

[44] X. Ma, M. Pu, X. Li, Y. Guo, P. Gao, and X. Luo, Meta-chirality: Fundamentals, construction and applications, Nanomaterials **7**, 116 (2017).

[45] T. T. Lv, Y. X. Li, H. F. Ma, Z. Zhu, Z. P. Li, C. Y. Guan, J. H. Shi, H. Zhang, and T. J. Cui, Hybrid metamaterial switching for manipulating chirality based on VO_2 phase transition, Sci. Rep. **6**, 23186 (2016).

[46] M. Hentschel, M. Schäferling, X. Duan, H. Giessen, and N. Liu, Chiral plasmonics, Sci. Adv. **3**, 5 (2017).

[47] J. Shi, Z. Li, D. K. Sang, Y. Xiang, J. Li, S. Zhang, and H. Zhang, THz photonics in two dimensional materials and metamaterials: Properties, devices and prospects, J. Mater. Chem. C **6**, 1291 (2018).

[48] J. B. Pendry, A chiral route to negative refraction, Science **306**, 1353 (2004).

[49] C. Monzon and D. W. Forester, Negative Refraction and Focusing of Circularly Polarized Waves in Optically Active Media, Phys. Rev. Lett. **95**, 123904 (2005).

[50] R.-L. Chern, Wave propagation in chiral media: Composite Fresnel equations, J. Opt. **15**, 075702 (2013).

[51] S. Zhang, Y.-S. Park, J. Li, X. Lu, W. Zhang, and X. Zhang, Negative Refractive Index in Chiral Metamaterials, Phys. Rev. Lett. **102**, 023901 (2009).

[52] Q. Cheng and T. J. Cui, Negative refractions in uniaxially anisotropic chiral media, Phys. Rev. B **73**, 113104 (2006).

[53] D. S. Borgnia, A. J. Kruchkov, and R.-J. Slager, Non-Hermitian Boundary Modes and Topology, Phys. Rev. Lett. **124**, 056802 (2020).

[54] M. Kim, Z. Jacob, and J. Rho, Recent advances in 2D, 3D and higher-order topological photonics, Light Sci. Appl. **9**, 130 (2020).

[55] M.-A. Miri and A. Alu, Exceptional points in optics and photonics, Science **9**, aar7709 (2019).

[56] A. Cerjan, S. Huang, M. Wang, K. P. Chen, Y. Chong, and M. C. Rechtsman, Experimental realization of a Weyl exceptional ring, Nat. Photonics **13**, 623 (2019).

[57] K. Takata and M. Notomi, Photonic Topological Insulating Phase Induced Solely by Gain and Loss, Phys. Rev. Lett. **121**, 213902 (2018).

[58] X.-W. Luo and C. Zhang, Higher-order topological corner states induced by gain and loss, Phys. Rev. Lett. **123**, 073601 (2019).

[59] J. Hou, Y.-J. Wu, and C. Zhang, Non-Hermitian topological phase transitions for quantum spin Hall insulators, Phys. Rev. B **103**, 205110 (2021).

[60] K. Kawabata, K. Shiozaki, M. Ueda, and M. Sato, Symmetry and Topology in Non-Hermitian Physics, Phys. Rev. X **9**, 041015 (2019).

[61] H. Hu, J. Hou, F. Zhang, and C. Zhang, Topological Triply Degenerate Points Induced by Spin-Tensor-Momentum Couplings, Phys. Rev. Lett. **120**, 240401 (2018).

[62] H. Shen, B. Zhen, and L. Fu, Topological Band Theory for Non-Hermitian Hamiltonians, Phys. Rev. Lett. **120**, 146402 (2018).

[63] Q. Yang, Y. Dong, W. Wu, C. Zhu, H. Chong, J. Lu, D. Yu, L. Liu, F. Lv, and S. Wang, Detection and differential diagnosis of colon cancer by a cumulative analysis of promoter methylation, Nat. Commun. **3**, 1206 (2012).

[64] X. Chen, C. Zhang, F. Yang, G. Liang, Q. Li, and L. J. Guo, Plasmonic lithography utilizing epsilon near zero hyperbolic metamaterial, ACS Nano **10**, 9863 (2017).

[65] X. Miao, D. Qu, D. Yang, B. Nie, Y. Zhao, H. Fan, Z. Sun, Photoluminescence: Synthesis of carbon dots with multiple color emission by controlled graphitization and surface functionalization, Adv. Mater. **30**, 1870002 (2018).

[66] R. Frank, Coherent control of Floquet-mode dressed plasmon polaritons, Phys. Rev. B **85**, 195463 (2012).

[67] R. Frank, Quantum criticality and population trapping of fermions by non-equilibrium lattice modulations, New J. Phys. **15**, 123030 (2013).

[68] R. Frank, Non-equilibrium polaritonics - non-linear effects and optical switching, Ann. Phys. (Berlin, Ger.) **525**, 66 (2012).

[69] A. Lubatsch and R. Frank, Quantum many-body theory for exciton-polaritons in semiconductor mie resonators in the non-equilibrium, Appl. Sci. **10**, 1836 (2020).

[70] A. Lubatsch and R. Frank, Evolution of Floquet topological quantum states in driven semiconductors, Eur. Phys. J. B **92**, 215 (2019).

[71] F. Wu, J. Guo, Y. Huang, K. Liang, L. Jin, J. Li, X. Deng, R. Jiao, Y. Liu, J. Zhang, W. Zhang, and L. Yu, Plexcitonic optical chirality: Strong exciton plasmon coupling in chiral J-aggregate-metal nanoparticle complexes, ACS Nano **15**, 2292 (2020).

[72] S. Schöche, P.-H. Ho, J. A. Roberts, S. J. Yu, J. A. Fan, and A. L. Falk, Mid-IR and UV-Vis-NIR Mueller matrix ellipsometry characterization of tunable hyperbolic metamaterials based on self-assembled carbon nanotubes, J. Vac. Sci. Technol. B **38**, 014015 (2020).

[73] M. Banders *et al.*, Topological insulator laser: Experiments, Science **359**, aar4005 (2018).

[74] M. Kim, P. Kang, J. Leem, and S. Nam, A stretchable crumpled graphene photodetector with plasmonically enhanced photoresponsivity, Nanoscale **9**, 4058 (2017).

[75] J. S. T. Smalley, F. Vallini, S. A. Montoya, L. Ferrari, S. Shahin, C. T. Riley, B. Kanté, E. E. Fullerton, Z. Liu, and Y. Fainman, Luminescent hyperbolic metasurfaces, Nat. Commun. **8**, 13793 (2017).

[76] J. Jung, H. Park, J. Park, T. Chang, and J. Shin, Broadband metamaterials and metasurfaces: A review from the perspectives of materials and devices, Nanophotonics **9**, 3165 (2020).